Pressure-Induced Indirect-Direct Bandgap Crossover and Bandgap Engineering in Ductile Semiconductor Ag_3PO_4 with Negative Linear Compressibility

Yang Lu[1], Shengcai Zhu[1,2], Eugene Huang[1], Yu He[1,3], Jiaji Ruan[1] & Hao Yan[1]

Silver orthophosphate (Ag_3PO_4) has aroused widespread interest since the discovery of visible-light-driven photocatalysis activity. However, its indirect bandgap nature at ambient becomes an obstacle to improve the photocatalysis efficiency and use in other application fields. In this study, the indirect-to-direct bandgap crossover was found during the pressure-induced phase transition from cubic to trigonal phase in Ag_3PO_4. The observed bandgap narrowing could be partially retained after pressure was released to ambient conditions, accelerating to efficiently utilize the solar spectrum. Moreover, Ag_3PO_4 was ductile like metals. Unexpectedly, this ion-conducting and ductile semiconductor photocatalyst further exhibited the negative linear compressibility (NLC) at pressure range of 7.5-25 GPa. This work, combining experimental and theoretical tools, provides an insight into the modulation mechanism of the electronic structure for silver-based semiconductors, and may broaden the applications of Ag_3PO_4.

[1]Center for High Pressure Science & Technology Advanced Research, Shanghai 201203, China. [2]Department of Physics and Astronomy, High Pressure Science and Engineering Center, University of Nevada Las Vegas, NV 89154, USA. [3]Key Laboratory of High-Temperature and High-Pressure Study of the Earth's Interior, Institute of Geochemistry, Chinese Academy of Sciences, Guiyang, Guizhou 550081, China. E-mail: yanhao@hpstar.ac.cn.

chinaXiv:201809.00002v1

chinaXiv:201809.00002v1

The direct and indirect bandgap characters of a semiconductor play a key role in photo-excited processes, including the separation, transfer, and recombination of photo-induced electrons and holes, which profoundly affect the physicochemical properties and the performances in applications.[1-3] For an indirect bandgap semiconductor, the optical absorption coefficients and the recombination are lower than in a direct semiconductor because the absorption involves not only the incident photons, but also phonons. Interestingly, indirect/direct bandgap crossover could balance the absorption and recombination and may further observe exotic phenomena, such as valley-based properties.[2,4] Recently, the crossover from indirect to direct bandgap was widely observed in monolayered materials with quantum confinement effect.[2,5-8] Applying tensile strain or rising temperature, the crossover can also be emerged in multilayered materials due to the decoupling interplay and lattice expansion.[9-11] Pressure is an effective approach to tune the crystal structure, lattice parameters, and electronic structure of materials.[12-14] Unfortunately, materials under pressure generally undergo a direct-to-indirect and not an indirect-to-direct bandgap transition, attributing to compressive effect.[15,16]

Silver ion conductors are a versatile class of materials with rich mechanical, optical, and transport properties.[17-25] Owing to the weak interplay of the Ag atoms with the environment, these materials are usually ductile under stress and possess excellent ionic conductivity, such as the soft semiconductor α-Ag_2S and super-ionic conductor α-AgI.[18,26-28] Recently, the discovery of the visible-light-driven photocatalytic activity of the ion-conducting Ag_3PO_4 semiconductor for water splitting for green energy has attracted much more interesting in the exploiting the silver-based photocatalysts.[19,20] Under Illumination with visible light (wavelength < 500 nm), this novel photocatalyst can yield an extremely high quantum efficiency of ~90% towards oxygen evolution.[19] However, the indirect bandgap nature of the Ag_3PO_4 semiconductor at ambient conditions may impede the improvement of absorption properties, which in turn lowers the photocatalytic efficiency. Furthermore, Ag_3PO_4 should possess good ductility like α-Ag_2S and other exotic properties for new applications.

In this work, combined with high-pressure experiments and density functional theory (DFT) calculations, we found that the indirect-to-direct bandgap crossover of Ag_3PO_4 under pressure couples with a phase transition from cubic to trigonal. Experimentally, the bandgap of Ag_3PO_4 narrowed from 2.37 eV to 1.82 eV via compression and the shrinking bandgap could be partially retained after releasing the pressure to ambient conditions. Besides, this material also exhibits good ductility and negative linear compressibility. Via the DFT calculation, we confirmed the high-pressure phase atomic structure, the indirect-to-direct bandgap crossover, and the bandgap narrowing. Our results will shed light on materials with a direct/indirect bandgap engineering under pressure and may promotes potential applications in new fields.

Results

High purity Ag_3PO_4 powder (Figure S1) was employed to study the ductility, atomic structure evolution, and electronic structure change through pressure treatments (Figure 1a). Upon pressurising, the yellow powder could be easily made into a sheet between the diamond culets, showing excellent ductility (Figure S2). Then, the pressure effects on the optical properties of this sheet-formed material were explored by *in situ* UV-vis absorption spectroscopy. Figure 1b and c show the absorption spectra of the typical Ag_3PO_4 slice under compression and decompression, respectively. As pressure increased from ambient to 50 GPa, the position of the absorption edge shows red-shifting from 500 nm to around 650 nm. Meanwhile, the slope of absorption edge clearly decreased when pressure exceeded 8.2 GPa, revealing the degeneration of the indirect bandgap and direct bandgap. At a pressure range from 18.9 GPa to 50 GPa, the slope has a subtly increasing trend (Figure S3), which may imply a direct-to-indirect bandgap transition. Upon decompression, the changes in position for the absorption edge as well as the slope are reversible.

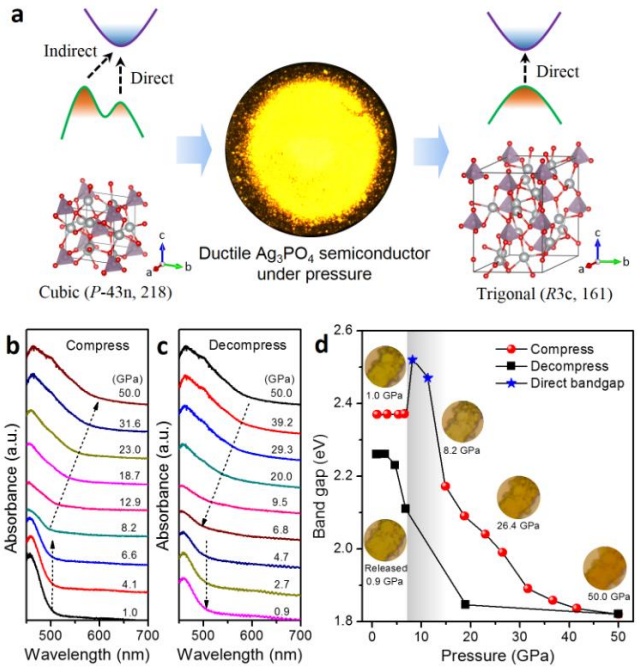

Figure 1. Optical properties of ductile Ag_3PO_4 semiconductor. (**a**) Scheme of crystal structure and indirect-to-direct transitions for ductile Ag_3PO_4 semiconductor by pressure treatment. (**b** and **c**) UV-vis absorption spectra of Ag_3PO_4 under compression and decompression, respectively. (**d**) Optical bandgap as a function of pressure. The indirect bandgap denoted by red (spherical) and black (square) data points, and the direct band gap denoted by the blue (star) data points.

The optical bandgap of Ag_3PO_4 as a function of pressure (Figure 1d) was derived from the absorption spectra via the Tauc method (Figure S4). The region with direct bandgap is marked by gray background between 7.5 GPa and 15 GPa. Below the critical pressure of 7.5 GPa, the indirect bandgap was 2.37 eV, agreeing with the previous report and remained stiff, which corresponds to the cubic phase.[19] In the gray region, the direct bandgap of Ag_3PO_4 with Trigonal-I phase jumped up to ~2.5 eV and then decreased with further increase in pressure. After the direct-to-indirect transition, the indirect bandgap of the sample monotonically narrowed to 1.82 eV with increasing pressure. Meanwhile, the color of the sample changed from yellow to orange during compression, as evidenced in the inserted photographs of the Ag_3PO_4 slice (Figure 1d). Upon decompression, the bandgap hysteretically broadened from 1.82 eV to 2.26 eV, whilst the color back to yellow. Unexpectedly, the bandgap of the quenched sample at ambient condition decreased by 5% compared with the starting material, which may lead to an enhancement of photocatalytic activity.

The structural evolution should dominate the variations of electronic structure, then the indirect/direct bandgap transitions and bandgap tuning under pressure. In this work, the Raman spectroscopy and angle-dispersive synchrotron X-ray diffraction (AD-XRD) experiments associated with theoretical calculations were conducted

under pressure to gain the local and global structure information. At ambient conditions, Ag_3PO_4 possesses a body-centered cubic structure (*P*-43n, No. 218) with a lattice parameter of ~6.01 Å.[29-31] In this structure, the regular [PO_4] tetrahedra, constituting the body-centered cubic lattice, are isolated by highly distorted [AgO_4] tetrahedra and each oxygen atom coordinates to one phosphorus atom and three silver atoms. Owing to the greater electronegativity of P relative to the Ag atom, the P-O bonds are stronger than the covalence-like Ag-O bonds. This then results in a prominent Raman peak at frequencies of 908 cm^{-1} for ambient Raman spectra (Figure S5a, b), which could be identified as the symmetry stretching vibration of [PO_4] tetrahedron.[32-35] In high-pressure Raman experiments, the vibration trended to a higher frequency with increasing pressure, except the turning range near 7.5 GPa with a red shift of 2 cm^{-1} (Figure S5a, b, d, e), which indicated the phase transition of Ag_3PO_4. Meanwhile, the prominent Raman peaks gradually broadened after a sharp jump around the phase transition point (Figure S5c, f), suggesting the slight distortion of the lattice under elevated pressure. During decompression to ambient pressure, the broadened Raman peaks could not be fully recovered, while the frequency of the [PO_4] phonon mode rapidly reverted to the original position except the hysteresis during the high-pressure phase.

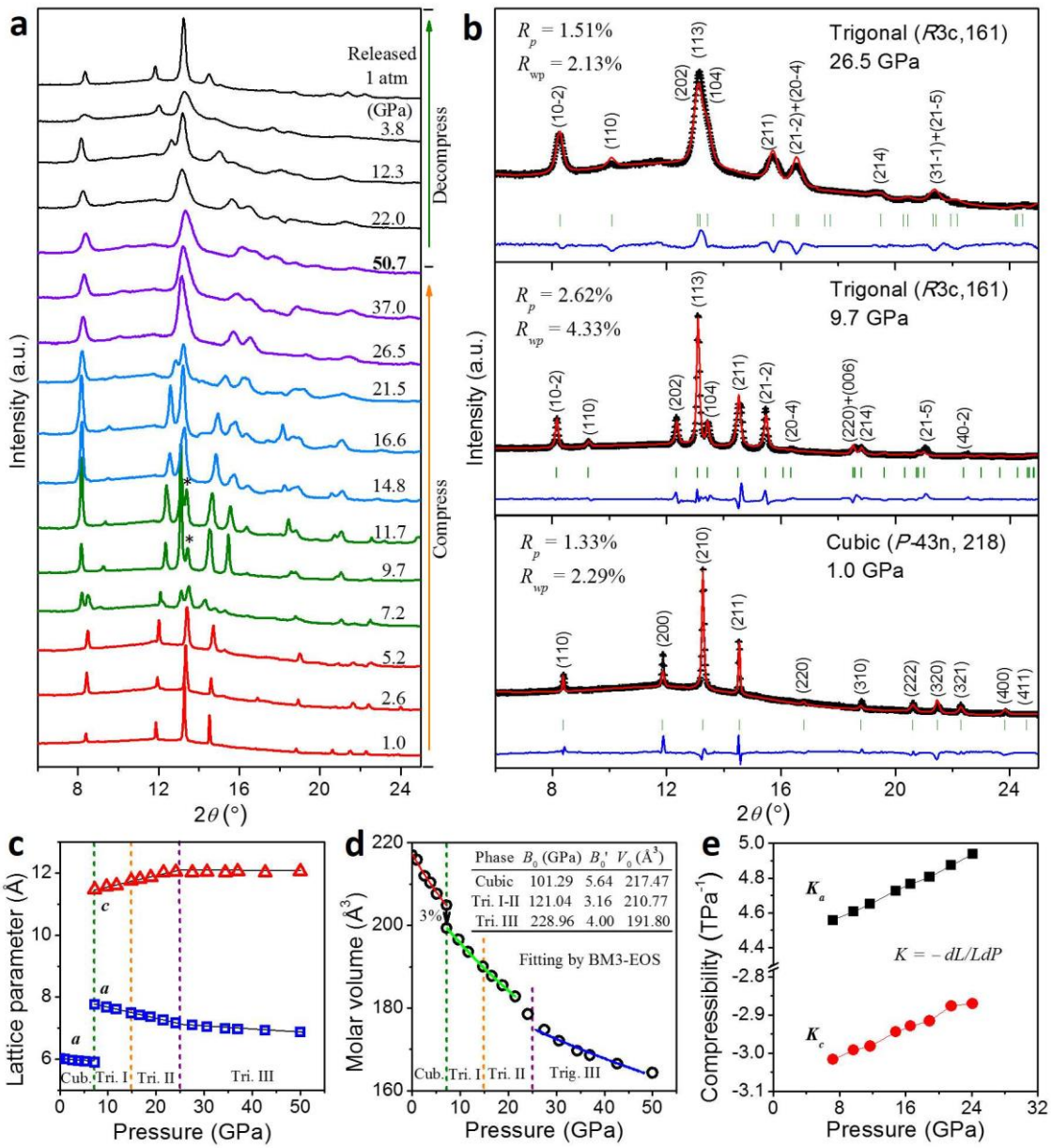

Figure 2. Pressure-induced structural evolution. (**a**) Synchrotron X-ray diffraction patterns of Ag_3PO_4 under both compression and decompression (λ = 0.6199 Å). (**b**) Rietveld refinements of the experimental (black fork) XRD data at 1.0 GPa, 9.7 GPa, and 26.5 GPa. The blue lines denote the difference between the experiments (black) and refinements (red), and the green vertical lines stand for the refined peak positions. (**c, d**) Pressure-dependent lattice parameters and molar volume of Ag_3PO_4. The relationship between the molar volume and pressure were fitted by the 3rd-order Birch-Murnaghan (BM3) equation of state (EOS) $P(V)=3B_0 f_E(1+2f_E)^{5/2}[1+\frac{3}{2}(B_0^{'}-4)f_E]$ where $f_E=[(V_0/V)^{2/3}-1]/2$ is the Eulerian strain, B_0 is the bulk modulus, $B_0^{'}$ is its pressure derivative, and V and V_0 are the unit cell volume and volume at zero pressure. (**e**) Variation of compressibility for the Trigonal I-II unit-cell axis as a function of pressure.

chinaXiv:201809.00002v1

Knowledge of the pressure-induced structural evolution can be gained from the synchrotron X-ray diffraction (XRD) spectra. Figure 2a shows the XRD patterns of Ag_3PO_4 under compression up to 50 GPa and decompression to ambient pressure. All the Bragg peaks shifted towards higher angles when pressure was applied up to 5.2 GPa due to the unit cell contraction, suggesting that the cubic structure of the low-pressure phase could survive above 5.2 GPa. Three trigonal phases (*R*3c, No. 161) appeared in the pressure range of 9.7-50.7 GPa. Particularly, the cubic and Trigonal-I phases coexisted around 7.2 GPa. A peak around the 13.5° (marked by the star in Figure 2a) gradually merged with the closed peak and disappeared under a pressure of 14.8 GPa, indicating another phase (Trigonal-II) transition occurred. Subsequently, the peaks at range of 12°-14° continue to merge into one peak when pressure up to 26.5 GPa, revealing the Trigonal-III phase emerging. Figure 2b shows the typical Rietveld refinements of the XRD patterns at 1.0 GPa, 9.7 GPa, and 26.5 GPa, respectively (Table S1 and S2). Obviously, the good refinements confirmed that Ag_3PO_4 underwent phase transitions from cubic to trigonal structures under high pressure. To our best knowledge, the pressure-induced phase transition from cubic to trigonal is, for the first time, observed in A_3BX_4–type compounds.

The crystal structure refinement parameters of all diffraction patterns are summarized in Figure 2c and d. The lattice parameters and molar volume of cubic Ag_3PO_4 decreased with increasing pressure. Unusually, the *c*-axis of the Trigonal-I and II (or Tri. I and Tri. II) phases exhibits negative linear compressibility with -3.02 ~ -2.87 TPa^{-1} (Figure 2c and e). Hence, the Ag_3PO_4, has the potential applications in highly sensitive pressure sensors, optical fibers with high shock resistance, and artificial muscles. The anisotropy of the compressive behavior should be ascribed to the relatively compact stacking along the <001> orientation and the distortion of the [AgO_x] polyhedron. After the transition from the Trigonal-II to Trigoanl-III phases around 26 GPa, the lattice parameter of *c* shows a steady, while *a* continues to decrease at a slower rate. From the volume-pressure relationship, as shown in Figure 2d, the percentage decreases of the molar volumes from the cubic to Trigonal-I phase around 7.5 GPa were calculated to be 3%. In addition, a 3rd-order Birch-Murnaghan (BM3) equation of state (EOS) was employed to fit the experimental data belonging to each structure. Then, the EOS parameters were determined to have a bulk modulus of B_0 = 101.29 GPa and volume of V_0 = 217.47 $Å^3$ for the cubic Ag_3PO_4, B_0 = 121.04 GPa and V_0 = 210.77 $Å^3$ for the Trigonal I-II structures, and B_0 = 228.96 GPa and V_0 = 191.80 $Å^3$ for the Trigonal-III structure. For cubic Ag_3PO_4, the bulk modulus is very small, suggesting that Ag_3PO_4 is very soft like some metals and the ductile semiconductor α-Ag_2S with a bulk modulus of 59.7 GPa.[26,36] Therefore, the semiconductor Ag_3PO_4 could be applied into the flexible devices, such as resistive random access memory.

After decompression to ambient pressure, the cubic structure of Ag_3PO_4 was recovered with hysteresis viewed from the shifted Bragg peaks, which agrees with Raman observation. This means that the pressure-induced phase transition of Ag_3PO_4 is partially reversible. Comparatively, the quenched sample possesses the same lattice parameter of 6.01 Å with the pristine sample, but with broadened peaks (Figure S6). Considering the rapid recovery of the [PO_4] tetrahedra from the high- to low-pressure phase (see Raman results), the hysteresis and broadening should be attributed to the slow movement of the silver atoms to their original positions in the cubic unit cell, which is related to the hysteresis of bandgap during compression.

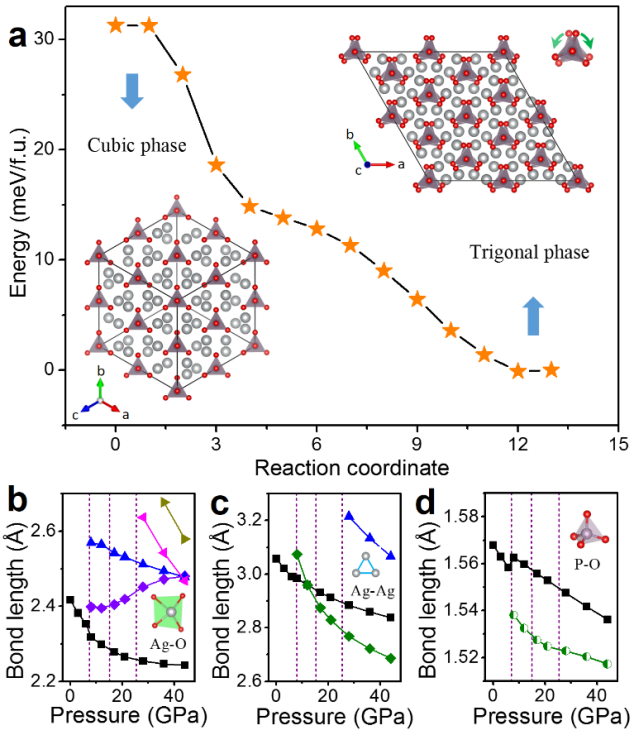

Figure 3. Mechanism and details of phase transitions. (**a**) Calculated enthalpy of the phase transition at 7.5 GPa. Insets are the pressure-induced structural change of the 2×2×2 unit cells viewed from the $[111]_{Cubic}$ // $[001]_{Trigonal}$ direction. (**b**, **c**, and **d**) Theoretical bond length of Ag-O, Ag-Ag, and P-O as a function of pressure, respectively.

To better understand the phase transition, theoretical calculations of Ag_3PO_4 were conducted using the Stochastic Surface Walking (SSW) method, which has been successful in the TiO_2 and FeOOH systems.[37-40] The pathway sampling was carried out initially using the VASP package starting from cubic Ag_3PO_4 (2 Ag_3PO_4 units per cell) to generate a database of pathways that connect Ag_3PO_4 with the other phases. In total, 120 pathways were collected from 500 SSW-crystal steps of pathway sampling. While the majority of pathways (80) were found to convert cubic Ag_3PO_4 to Trigonal-I phase, other pathways leading to phases such as monoclinic were also identified. The first principles DFT calculations based on the variable-cell double-ended surface walking method[38] were then utilized to verify the energetics of every low-energy pathways, from which the lowest energy reaction pathway is obtained. The lowest energy pathway leaving the cubic Ag_3PO_4 phase is the connection between the cubic Ag_3PO_4 and Trigonal-I phase, which is a one-step transition, and the other transition pathways leaving the cubic Ag_3PO_4 phase are energetically much higher. The reaction profile is shown in Figure 3a, starting from a cubic Ag_3PO_4 lattice to a Trigonal-I phase lattice. Wefound the phase transition is much simpler with only the [PO_4] polyhedrons rotated. To our surprise, the phase transition barrier from the cubic phase to Trigonal-I phase is almost zero calculated by the NEB method. This was indeed observed in our XRD experiment, where the phase transition takes place at 7.5 GPa. Furthermore, the calculated XRD patterns and volume-pressure relationship are consistent with the experimental results (Figure S7 and S8).

The phase transition of the Ag_3PO_4 from cubic to trigonal phases was schematically shown in the insets of Figure 3a, viewed from the $[111]_{Cubic}$ // $[001]_{Trigonal}$ orientation. Apparently, the applied pressure induced the change of the [AgO_4] polyhedrons, then resulted in the reversed rotation with around 10° for alternative [PO_4] tetrahedrons along the $[111]_{Cubic}$ // $[001]_{Trigonal}$ direction. To obtain more details, the calculated bond lengths of Ag-O, Ag-Ag, and P-O of Ag_3PO_4 under pressure are summarized in Figure 3b-d. Obviously, all the bond lengths split due to the rearrangement of atoms after the cubic-trigonal transition, revealing the symmetry breakage of the [AgO_x] polyhedron. As pressure increased, the bonds of

chinaXiv:201809.00002v1

the trigonal phase generally shrunk. Notably, one of the P-O bonds of the cubic and trigonal phases narrowed linearly with increasing pressure, which is reflected in the Raman vibration (Figure 3d and S5). On the other hand, along the $[001]_{Trigonal}$ direction, the regular $[PO_4]$ tetrahedrons were slightly squashed by 1-2% and the $[AgO_x]$ polyhedrons underwent a huge distortion, resulting in the compact stacking of Ag_3PO_4 trigonal structures.

To gain insight into the substantial correlation of the crystal structure with optical properties, the electronic band structures of Ag_3PO_4 with different phases were calculated using the DFT method. It is well known that the common exchange-correlation functionals, such as the LDA and GGA, are severely underestimated in the bandgap. In order to overcome this, we used PBE0 hybrid exchange-correlation functional to calculate the band structure. As shown in Figure 4a, the bandgap at ambient pressure is 2.42 eV, which is very consistent with 2.37 eV experiment. On another hand, the energy band configurations of the cubic and trigonal phases are very different, implying their distinction in optical properties. In detail, the indirect bandgap of the cubic phase at 0 GPa degenerated to a direct bandgap at 8 GPa after the phase transition from the cubic to Trigonal-I phase. As pressure increased more than 17 GPa, the indirect bandgap reappeared in the Trigonal-II and III phases. Figure 4b summarizes the pressure-dependent indirect and direct bandgap of Ag_3PO_4. Obviously, the energy difference between the direct and indirect bandgap for Ag_3PO_4 decreased from ~120 meV to 0 eV when the cubic phase shifted to Trigonal-I. Subsequently, the difference gradually increased to ~80 eV at 44 GPa for the Trigonal-III phase. The indirect/direct bandgap evolution trend agrees with the experimental results.

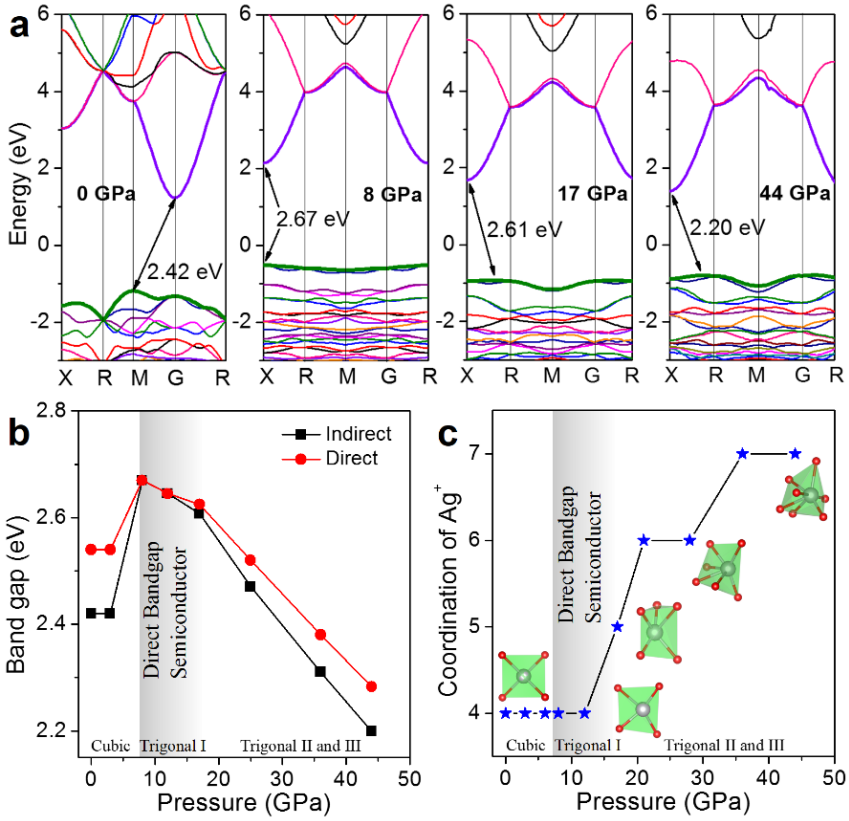

Figure 4. Electronic band structure and relation with the coordination of silver. (**a**) Calculated band structures for Ag_3PO_4 with cubic phase (0 GPa) and trigonal phases of I (8 GPa), II (17 GPa), and III (44 GPa). (**b**) Theoretical direct/indirect bandgap of Ag_3PO_4 as a function of pressure. (**c**) Pressure-induced coordination change of silver in $[AgO_x]$ polyhedrons.

The indirect-to-direct bandgap crossover usually occurs in transition metal dichalcogenides from bulk to a few-layers especially to monolayer, such as MoS_2, which originated from the quantum confinement effect.[3,5-7] Besides, the applied tensile strain and temperature rise can also effectively drive the bandgap crossover, from indirect to direct via the common effect of crystal lattice expansion.[9-11] In contrast, pressure generally results in the shrinking of the crystal cell and the coupling of neighboring atoms, then a direct-to-indirect bandgap transition, such as CdSe and $CsPbBr_3$ under pressure.[15,16] In our case, the direct-to-indirect bandgap transition of trigonal Ag_3PO_4 under higher pressure verified the pressure effect on the electronic structure. However, it is anomalous that the pressure-induced indirect-to-direct bandgap crossover during the phase transition from cubic to Trigonal-I phase.

The yellow Ag_3PO_4 can be treated as the black Ag_2O added with *p*-block phosphorus element based on the theoretical calculation.[19] Hence, the size and configuration evolutions of the $[AgO_x]$ polyhedron under pressure should dominate the electronic band structure and the optical properties. Therefore, the prolonged partial Ag-O and Ag-Ag bonds owing to the bond length splitting (Figure 3b and c) may primarily degenerate the indirect and direct bandgap after the cubic to trigonal phase transition. Based on the structural prediction, the coordination number of Ag^+ and the scheme of the $[AgO_x]$ group as a function of pressure were obtained and are shown in Figure 4c. Apparently, the silver coordination of the Trigonal-I phase is equal to that of the cubic phase, but varies the $[AgO_4]$ structure and breaks its centrosymmetry. When pressure rises up to 44 GPa, the silver coordination increases from 4 to 7, accompanying the growing complexity of the $[AgO_x]$ configuration. Comparatively, the transitions between the indirect and direct bandgap for Ag_3PO_4 display a good correlation with the Ag^+ coordination number and $[AgO_x]$ configuration.

In conclusion, the pressure modulations in the crystal structure and optical properties of ductile Ag_3PO_4 semiconductor were systematically studied by *in situ* synchrotron X-ray diffraction and optical absorption

chinaXiv:201809.00002v1

spectroscopy combined with theoretical calculations. Under compression, the indirect bandgap Ag_3PO_4 semiconductor exhibited a good ductility and underwent a reversible phase transitions. The pressure-induced phase transition from cubic to trigonal phases in Ag_3PO_4 are, for the first time, observed in A_3BX_4–type compounds. The bandgap of Ag_3PO_4 was narrowed from 2.37 eV to 1.82 eV via compression and the shrinking band gap could be partially retained after releasing the pressure to ambient pressure. In addition, an indirect-to-direct bandgap crossover was found during the phase transition from cubic to the first trigonal structures as predicted by theoretical calculations. At much higher pressure, the transition from direct to indirect bandgap was strongly correlated to the weakening in bonds and increased Ag^+ coordination number. These results may provide clues for the understanding of underlying mechanism that causes the tuning of the electronic band structure and furnish the opportunity in the design of better functional materials.

Methods

Diamond anvil cell sample loading. Silver orthophosphate powder (Ag_3PO_4, Alfa Aesar, 99%) was loaded into a Mao-Bell type symmetric diamond anvil cell (DAC, 300 μm culets) with a ruby chip for pressure determinations. T301 stainless steel or Rhenium foil (250 μm in thickness) was pre-indented to 40 μm in thickness and a hole was laser drilled (λ = 1064 nm, Power < 0.3 W) at the indentation center to serve as the gasket and sample chamber. Silicone oil was employed as the pressure-transmitting medium (PTM). The pressures were measured with the *in situ* ruby fluorescence technique.[41]

***In situ* high-pressure structural characterizations.** The *in situ* high-pressure angle-dispersive X-ray diffraction (AD-XRD) experiments were executed in the Shanghai Synchrotron Radiation Facility (SSRF, BL15U1), Advanced Light Source (ALS, BL12.2.2), and Stanford Synchrotron Radiation Lightsource (SSRL, BL10-2) with wavelengths of 0.6199, 0.49594, and 0.6199 Å. The resulting two-dimensional patterns were integrated using Fit2D software.[42] Rietveld refinements were performed using the General Structure Analysis System (GSAS) with the user interface EXPGUI package.[43,44] The *in situ* high-pressure Raman spectroscopy experiments were performed on a Raman spectroscopy system in the backscattering configuration with an excitation laser (λ = 532 nm, Renishaw 1000).

***In situ* high-pressure optical measurements.** The powdered Ag_3PO_4 sample was pressurised (up to 3 GPa) by DAC without PTM to form a film with a thickness of ~10 μm. Two pieces of film were peeled off the diamond culet and together with a ruby chip were loaded into the DAC sample chamber, using silicone oil as PTM. The high-pressure UV-vis spectroscopy measurements were carried out by a micro UV-vis spectroscopy system (DH-2000-BAL, Ocean Optics). During compression and decompression, the Ag_3PO_4 sample color change was photographed by optical microscope (Leica M205C).

Stochastic Surface Walking (SSW) Global Structure Search. The PES of Ag_3PO_4 was explored using a DFT based SSW global structure search (SSW-DFT). The SSW method[45,46] is an unbiased, automated approach to explore the multidimensional PES of complex systems by taking into account the second derivative information[47]. The efficiency of the method for exploring PES has been demonstrated for both aperiodic (molecules[48] and clusters[49]) and periodic (surfaces[50], crystals[51-54]) systems. The algorithm of the SSW global optimization method can be found in reference. In detail, the potential energy surface of Ag_3PO_4 was carried out in a 16-atom (2 Ag_3PO_4 units per cell) Ag_3PO_4 lattice, using the cubic structures of Ag_3PO_4 as seeds, which is the most stable phase at ambient conditions at 10 GPa. In the SSW search, we generally performed a series of parallel runs (4−10 depending on the system) starting from the initial guess structures, and up to 300 minima were collected at the first stage, from which the most stable configuration was obtained. Next, we verified the result with the experiment results. If the most stable configuration of the first stage was inconsistent with the experiment, then another 300 minima were collected. This process was repeated until the configuration is consistent with the experiment. Via the ransom search, we found the most stable configuration, which agreed well with the experiment (see the following section).

SSW pathway sampling. The SSW algorithm has an automated climbing mechanism to drive an atomic configuration from a local energy-minimum state to a high-energy configuration along random directions, inheriting the idea of the bias-potential driven constrained-Broyden-dimer (BP-CBD) method for the transition-state (TS) location.[55] Three steps are involved for finding the lowest energy pathway, as described below briefly. **(i) Pathway collection** In SSW pathway sampling, first, we start from one single phase (starting phase), and utilize the SSW method to explore all the likely phases nearby the phase. A structure selection module is utilized to decide whether to accept/refuse once a new minimum is reached. If the new phase that is different from the starting phase is identified by the SSW crystal method[56], we record/output the IS (i.e. starting phase) and the FS (a new phase) of the current SSW step. Then, the program will return to the IS by rejecting the new minimum to continue the phase exploration; On the other hand, if the new minimum identified by SSW is still the starting phase (e.g., the same symmetry but a permutation isomer with varied lattice), the program will accept the new isomeric phase and start the phase exploration from this phase. We repeated this procedure until a certain number of IS/FS pairs were reached. **(ii) Pathway screening** Secondly, we utilized the variable-cell double-ended surface walking (DESW) method[57] to establish the pseudopathway connecting IS to FS for all IS/FS pairs[58,59]. The approximate barrier is obtained according to DESW pseudopathway, where the maximum energy point along the pathway is generally a good estimate for the true TS[57]. By sorting the approximate barrier height, we can obtain the candidates for the lowest energy pathways. **(iii) Lowest energy pathway determination** Thirdly, the candidate lowest energy pathways are selected to exactly locate the *true* TS by using the DESW TS-search method[57]. By sorting the exact barrier calculated, the energy difference between the TS and the IS, the lowest energy pathways could be finally obtained. All the lowest energy pathways will be further confirmed by extrapolating TS towards IS and FS, and the TSs need to be validated by phonon spectrum calculation, showing one and only one imaginary mode. In this study, we explore the structural transformation between the cubic Ag_3PO_4 phase and the high-pressure Ag_3PO_4 phases, using the SSW method. Based on the sampled free energy landscape, the pathways connecting the initial structure and the final structure on the potential energy surface can be determined in an atom-to-atom correspondence, and we further export the pathway by the nudged elastic band (NEB) method[60].

DFT calculation details. All calculations were performed using the plane-wave DFT program, Vienna *ab initio* simulation package (VASP)[61] where the electron-ion interaction of Ag, P, and O atoms are represented by the projector augmented wave[62] (PAW) scheme and the exchange-correlation functional assumes the GGA-PBE type[63]. In the SSW pathway sampling, 16-atom Ag_3PO_4 supercells (both ε and Py phase) at 10 GPa were used. In order to speed up the PES exploration, we adopted the following parameter setting: the kinetic energy plane-wave cutoff 400 eV; and the Monkhorst-Pack k-point mesh of (4×4×4) for 16-atom supercells. Once the low-energy pathways were located, we switched to high-accuracy calculations using a plane-wave cutoff of 800 eV and a denser Monkhorst-Pack *k*-point mesh (8×8×8) for 16-atom supercells. For all the structures, both the lattice and atomic positions were fully optimized until the maximal stress component was below 0.1 GPa and the maximal force component was below 0.01 eV/Å. It is well known that GGA severely underestimate bandgaps, thus we calculated the density of states using the PBE0 hybrid exchange-correlation functional.[64]

chinaXiv:201809.00002v1

References

1 Hutter, E. M. *et al.* Direct-indirect character of the bandgap in methylammonium lead iodide perovskite. *Nat Mater* **16**, 115-120, doi:10.1038/nmat4765 (2017).

2 Wang, Q. H., Kalantar-Zadeh, K., Kis, A., Coleman, J. N. & Strano, M. S. Electronics and optoelectronics of two-dimensional transition metal dichalcogenides. *Nat Nanotechnol* **7**, 699-712, doi:10.1038/nnano.2012.193 (2012).

3 Zhang, Y. *et al.* Direct observation of the transition from indirect to direct bandgap in atomically thin epitaxial MoSe2. *Nat Nanotechnol* **9**, 111-115, doi:10.1038/nnano.2013.277 (2014).

4 Mai, C. *et al.* Many-body effects in valleytronics: direct measurement of valley lifetimes in single-layer MoS2. *Nano Lett.* **14**, 202-206, doi:10.1021/nl403742j (2014).

5 Mak, K. F., Lee, C., Hone, J., Shan, J. & Heinz, T. F. Atomically ThinMoS2: A New Direct-Gap Semiconductor. *Phys. Rev. Lett.* **105**, doi:10.1103/PhysRevLett.105.136805 (2010).

6 Splendiani, A. *et al.* Emerging photoluminescence in monolayer MoS2. *Nano Lett.* **10**, 1271-1275, doi:10.1021/nl903868w (2010).

7 Kuc, A., Zibouche, N. & Heine, T. Influence of quantum confinement on the electronic structure of the transition metal sulfideTS2. *Physical Review B* **83**, doi:10.1103/PhysRevB.83.245213 (2011).

8 Zhang, S., Yan, Z., Li, Y., Chen, Z. & Zeng, H. Atomically thin arsenene and antimonene: semimetal-semiconductor and indirect-direct band-gap transitions. *Angew. Chem. Int. Ed. Engl.* **54**, 3112-3115, doi:10.1002/anie.201411246 (2015).

9 Tongay, S. *et al.* Thermally driven crossover from indirect toward direct bandgap in 2D semiconductors: MoSe2 versus MoS2. *Nano Lett.* **12**, 5576-5580, doi:10.1021/nl302584w (2012).

10 Desai, S. B. *et al.* Strain-induced indirect to direct bandgap transition in multilayer WSe2. *Nano Lett.* **14**, 4592-4597, doi:10.1021/nl501638a (2014).

11 Yun, W. S., Han, S. W., Hong, S. C., Kim, I. G. & Lee, J. D. Thickness and strain effects on electronic structures of transition metal dichalcogenides: 2H-MX2semiconductors (M=Mo, W;X=S, Se, Te). *Physical Review B* **85**, doi:10.1103/PhysRevB.85.033305 (2012).

12 Mao, H.-K., Chen, X.-J., Ding, Y., Li, B. & Wang, L. Solids, liquids, and gases under high pressure. *Reviews of Modern Physics* **90**, doi:10.1103/RevModPhys.90.015007 (2018).

13 Zhang, L., Wang, Y., Lv, J. & Ma, Y. Materials discovery at high pressures. *Nature Reviews Materials* **2**, doi:10.1038/natrevmats.2017.5 (2017).

14 Jaffe, A., Lin, Y., Mao, W. L. & Karunadasa, H. I. Pressure-Induced Metallization of the Halide Perovskite (CH3NH3)PbI3. *J. Am. Chem. Soc.* **139**, 4330-4333, doi:10.1021/jacs.7b01162 (2017).

15 Tolbert, S. H., Herhold, A. B., Johnson, C. S. & Alivisatos, A. P. Comparison of Quantum Confinement Effects on the Electronic Absorption Spectra of Direct and Indirect Gap Semiconductor Nanocrystals. *Phys. Rev. Lett.* **73**, 3266-3269, doi:10.1103/PhysRevLett.73.3266 (1994).

16 Xiao, G. *et al.* Pressure Effects on Structure and Optical Properties in Cesium Lead Bromide Perovskite Nanocrystals. *J. Am. Chem. Soc.* **139**, 10087-10094, doi:10.1021/jacs.7b05260 (2017).

17 Aboagye, J. K. & Friauf, R. J. Anomalous high-temperature ionic conductivity in the silver halides. *Physical Review B* **11**, 1654-1664, doi:10.1103/PhysRevB.11.1654 (1975).

18 Mellander, B. E. Electrical conductivity and activation volume of the solid electrolyte phaseα-AgI and the high-pressure phase fcc AgI. *Physical Review B* **26**, 5886-5896, doi:10.1103/PhysRevB.26.5886 (1982).

19 Yi, Z. *et al.* An orthophosphate semiconductor with photooxidation properties under visible-light irradiation. *Nat Mater* **9**, 559-564, doi:10.1038/nmat2780 (2010).

20 Bi, Y., Ouyang, S., Umezawa, N., Cao, J. & Ye, J. Facet effect of single-crystalline Ag3PO4 sub-microcrystals on photocatalytic properties. *J. Am. Chem. Soc.* **133**, 6490-6492, doi:10.1021/ja2002132 (2011).

21 Kahk, J. M. *et al.* The electronic structure of silver orthophosphate: experiment and theory. *J. Mater. Chem. A* **2**, 6092-6099, doi:10.1039/c3ta14191h (2014).

22 Teng, F., Liu, Z., Zhang, A. & Li, M. Photocatalytic Performances of Ag3PO4 Polypods for Degradation of Dye Pollutant under Natural Indoor Weak Light Irradiation. *Environ. Sci. Technol.* **49**, 9489-9494, doi:10.1021/acs.est.5b00735 (2015).

23 Roca, R. A. *et al.* Formation of Ag Nanoparticles on beta-Ag2WO4 through Electron Beam Irradiation: A Synergetic Computational and Experimental Study. *Inorg. Chem.* **55**, 8661-8671, doi:10.1021/acs.inorgchem.6b01215 (2016).

24 Silva, G. S. *et al.* Theoretical and Experimental Insight on Ag2CrO4 Microcrystals: Synthesis, Characterization, and Photoluminescence Properties. *Inorg. Chem.* **55**, 8961-8970, doi:10.1021/acs.inorgchem.6b01452 (2016).

25 Takahashi, T., Ikeda, S. & Yamamoto, O. Solid-state ionics - solids with high ionic conductivity in the systems silver iodide--silver oxyacid salts. *J. Electrochem. Soc.; (United States)* **119:4** (1972).

26 Shi, X. *et al.* Room-temperature ductile inorganic semiconductor. *Nat Mater* **17**, 421-426, doi:10.1038/s41563-018-0047-z (2018).

27 Arima, H. *et al.* In situ XAFS and XRD studies of pressure-induced local structural change in liquid AgI. *J Phys Condens Matter* **19**, 076104, doi:10.1088/0953-8984/19/7/076104 (2007).

28 Hao, A. *et al.* Conductivity of AgI under high pressure. *J. Appl. Phys.* **101**, 053701, doi:10.1063/1.2709579 (2007).

29 Wyckoff, R. W. G. Crystal structure of silver phosphate and silver arsenate. (1925).

30 Helmholz, L. The Crystal Structure of Silver Phosphate. *J. Chem. Phys.* **4**, 316-322 (1936).

31 Ng, H. N., Calvo, C. & Faggiani, R. A new investigation of the structure of silver orthophosphate. *Acta Crystallogr.* **34**, 898–899 (1978).

32 Lopez-Bote, M. A. & Montero, S. Raman intensities, vibrational eigenvectors, electro-optical parameters and force constants of SO42−, ClO4−, PO43, CO32− and NO3− anions in polycrystalline samples. *J. Raman Spectrosc.* **9**, 386–392 (1980).

33 Boily, J. F. Intramolecular Bonding and Charge Distributions in XO4 (X = Si, P, S, Cl and Ge, As, Se, Br) Oxyanions from Topological Analyses of the Electron Density. *J. Phys. Chem. A* **106**, 4718-4724 (2002).

34 Dong, P. *et al.* Ag3PO4/reduced graphite oxide sheets nanocomposites with highly enhanced visible light photocatalytic activity and stability. *Applied Catalysis B: Environmental* **132-133**, 45-53, doi:10.1016/j.apcatb.2012.11.022 (2013).

35 Wang, Z. *et al.* Synthesis and characterization of Ag3PO4/multiwalled carbon nanotube composite photocatalyst with enhanced photocatalytic activity and stability under visible light. *Journal of Materials Science* **49**, 1585-1593, doi:10.1007/s10853-013-7841-4 (2013).

36 Wang, P., Zhao, R., Wu, L. & Zhang, M. Effect of Y doping on high-pressure behavior of Ag2S nanocrystals. *RSC Advances* **7**, 35105-35110, doi:10.1039/c7ra05327d (2017).

37 Shang, C. & Liu, Z. P. Stochastic Surface Walking Method for Structure Prediction and Pathway Searching. *J Chem Theory Comput* **9**, 1838-1845, doi:10.1021/ct301010b (2013).

38 Zhang, X. J., Shang, C. & Liu, Z. P. Double-Ended Surface Walking Method for Pathway Building and Transition State Location of Complex Reactions. *Journal of Chemical Theory and Computation* **9**, 5745-5753 (2013).

39 Zhu, S. C., Hu, Q., Mao, W. L., Mao, H. K. & Sheng, H. Hydrogen-Bond Symmetrization Breakdown and Dehydrogenation Mechanism of FeO2H at High Pressure. *J. Am. Chem. Soc.* **139**, 12129 (2017).

40 Zhu, S. C., Xie, S. H. & Liu, Z. P. Nature of Rutile Nuclei in Anatase-to-Rutile Phase Transition. *J. Am. Chem. Soc.* **137**, 11532 (2015).

41 Mao, H. K., Xu, J. & Bell, P. M. Calibration of the ruby pressure gauge to 800 kbar under quasi-hydrostatic conditions. *Journal of Geophysical Research Solid Earth* **91**, 4673-4676 (1986).

42 Hammersley, A. P., Svensson, S. O., Hanfland, M., Fitch, A. N. & Hausermann, D. Two-dimensional detector software: From real

chinaXiv:201809.00002v1

detector to idealised image or two-theta scan. *High Pressure Research* **14**, 14 (1996).

43 Larson AC, V. D. R. General Structure Analysis System (GSAS). *Los Alamos National Laboratory Report LAUR (The Regents of the University of California, Los Alamos, NM)*, 86-748 (1994).

44 Toby, B. H. EXPGUI , a graphical user interface for GSAS. *J. Appl. Crystallogr.* **34**, 210–213 (2001).

45 Zhang, X. J., Shang, C. & Liu, Z. P. From Atoms to Fullerene: Stochastic Surface Walking Solution for Automated Structure Prediction of Complex Material. *J. Chem. Theory Comput.* **9**, 3252-3260, doi:10.1021/ct400238j (2013).

46 Shang, C. & Liu, Z. P. Stochastic Surface Walking Method for Structure Prediction and Pathway Searching. *J. Chem. Theory Comput.* **9**, 1838-1845, doi:10.1021/ct301010b (2013).

47 Guan, S. H., Zhang, X. J. & Liu, Z. P. Energy Landscape of Zirconia Phase Transitions. *J. Am. Chem. Soc.* **137**, 8010-8013, doi:10.1021/jacs.5b04528 (2015).

48 Zhang, X.-J. & Liu, Z.-P. Reaction sampling and reactivity prediction using the stochastic surface walking method. *Physical Chemistry Chemical Physics* **17**, 2757-2769 (2015).

49 Wei, G.-F. & Liu, Z.-P. Restructuring and hydrogen evolution on Pt nanoparticle. *Chemical Science* **6**, 1485-1490 (2015).

50 Zhu, S.-C., Xie, S.-H. & Liu, Z.-P. Nature of rutile nuclei in anatase-to-rutile phase transition. *Journal of the American Chemical Society* **137**, 11532-11539 (2015).

51 Zhu, S. C., Xie, S. H. & Liu, Z. P. Design and Observation of Biphase TiO_2 Crystal with Perfect Junction. *J. Phys. Chem. Lett.* **5**, 3162-3168, doi:10.1021/jz5016247 (2014).

52 Guan, S. H., Zhang, X. J. & Liu, Z. P. Energy Landscape of Zirconia Phase Transitions. *J. Am. Chem. Soc.* **137**, 8010 (2015).

53 Li, Y. F., Zhu, S. C. & Liu, Z. P. Reaction Network of Layer-to-Tunnel Transition of MnO_2. *J. Am. Chem. Soc.* **138**, 5371-5379 (2016).

54 Zhu, S.-c., Hu, Q., Mao, W. L., Mao, H.-k. & Sheng, H. Hydrogen-bond symmetrization breakdown and dehydrogenation mechanism of FeO2H at high pressure. *J. Am. Chem. Soc.* **139**, 12129-12132 (2017).

55 Shang, C. & Liu, Z. P. Constrained Broyden Dimer Method with Bias Potential for Exploring Potential Energy Surface of Multistep Reaction Process. *J. Chem. Theory Comput.* **8**, 2215-2222, doi:10.1021/ct300250h (2012).

56 Shang, C., Zhang, X. J. & Liu, Z. P. Stochastic surface walking method for crystal structure and phase transition pathway prediction. *Phys. Chem. Chem. Phys.* **16**, 17845-17856, doi:10.1039/c4cp01485e (2014).

57 Zhang, X.-J., Shang, C. & Liu, Z.-P. Double-Ended Surface Walking Method for Pathway Building and Transition State Location of Complex Reactions. *J.Chem.Theory Comput* **9**, 5745-5753, doi:10.1021/ct4008475 (2013).

58 Shang, C. & Liu, Z. P. Constrained Broyden Dimer Method with Bias Potential for Exploring Potential Energy Surface of Multistep Reaction Process. *J. Chem. Theory Comput.* **8**, 2215-2222, doi:10.1021/ct300250h (2012).

59 Shang, C. & Liu, Z.-P. Constrained Broyden Minimization Combined with the Dimer Method for Locating Transition State of Complex Reactions. *J. Chem. Theory Comput.* **6**, 1136-1144, doi:10.1021/ct9005147 (2010).

60 Sheppard, D., Xiao, P., Chemelewski, W., Johnson, D. D. & Henkelman, G. A generalized solid-state nudged elastic band method. *J. Chem. Phys.* **136**, 074103 (2012).

61 Kresse, G. & Furthmuller, J. Efficient iterative schemes for ab initio total-energy calculations using a plane-wave basis set. *Phys. Rev. B* **54**, 11169-11186, doi:10.1103/PhysRevB.54.11169 (1996).

62 Blochl, P. E. Projector Augmented-Wave Method. *Phys. Rev. B* **50**, 17953-17979, doi:10.1103/PhysRevB.50.17953 (1994).

63 Perdew, J. P., Burke, K. & Ernzerhof, M. Generalized gradient approximation made simple. *Phys. Rev. Lett.* **77**, 3865-3868, doi:10.1103/PhysRevLett.77.3865 (1996).

64 Perdew, J. P., Ernzerhof, M. & Burke, K. Rationale for mixing exact exchange with density functional approximations. *The Journal of chemical physics* **105**, 9982-9985 (1996).

Acknowledgements

This work was financially supported by the National Natural Science Foundation of China (NSFC) (Grant No. U1530402 and 21703004). We are grateful to the Shanghai Synchrotron Radiation Facility (SSRF), Advanced Light Source (ALS), and Stanford Synchrotron Radiation Lightsource (SSRL) for use of their facilities. We also acknowledge Prof. Yongjae Lee for sharing the synchrotron beam-time of SSRL, Prof. Lin Wang for using their UV-VIS spectrometer, and Dr. Jinfu Shu for helping in high pressure experiments.

ORCID

Yang Lu: 0000-0003-0019-061X

chinaXiv:201809.00002v1